ARTICLE IN PRESS

Nature Communications

https://doi.org/10.1038/s41467-026-73062-8

Article in Press

Global patterns of urban heat shaped by climate and morphology

Received: 2 December 2025

Accepted: 30 April 2026

[redacted]

Cite this article as: Lee, S., Yoo, C., Son, B. *et al.* Global patterns of urban heat shaped by climate and morphology. *Nat Commun* (2026). https://doi.org/10.1038/s41467-026-73062-8

Siwoo Lee, Cheolhee Yoo, Bokyung Son, Dongjin Cho, Jungho Im & T. C. Chakraborty

We are providing an unedited version of this manuscript to give early access to its findings. Before final publication, the manuscript will undergo further editing. Please note there may be errors present which affect the content, and all legal disclaimers apply.

If this paper is publishing under a Transparent Peer Review model then Peer Review reports will publish with the final article.

ARTICLE IN PRESS

© The Author(s) 2026. **Open Access** This article is licensed under a Creative Commons Attribution-NonCommercial-NoDerivatives 4.0 International License, which permits any non-commercial use, sharing, distribution and reproduction in any medium or format, as long as you give appropriate credit to the original author(s) and the source, provide a link to the Creative Commons licence, and indicate if you modified the licensed material. You do not have permission under this licence to share adapted material derived from this article or parts of it. The images or other third party material in this article are included in the article's Creative Commons licence, unless indicated otherwise in a credit line to the material. If material is not included in the article's Creative Commons licence and your intended use is not permitted by statutory regulation or exceeds the permitted use, you will need to obtain permission directly from the copyright holder. To view a copy of this licence, visit http://creativecommons.org/licenses/by-nc-nd/4.0/.

Global patterns of urban heat shaped by climate and morphology

Siwoo Lee[1, †], Cheolhee Yoo[2, 3, †], Bokyung Son[1], Dongjin Cho[4], Jungho Im[1, 5, 6, *], and TC Chakraborty[7]

[1] Department of Civil, Urban, Earth, and Environmental Engineering, Ulsan National Institute of Science and Technology (UNIST), Ulsan, South Korea

[2] Smart City Convergence Major, Pusan National University, Busan, South Korea

[3] Department of Urban Planning and Engineering, Pusan National University, Busan, South Korea

[4] Environmental Planning Institute, Seoul National University, Seoul, South Korea

[5] Graduate School of Artificial Intelligence, UNIST, Ulsan, South Korea

[6] Graduate School of Carbon Neutrality, UNIST, Ulsan, South Korea

[7] Pacific Northwest National Laboratory, Richland, WA, USA

* Corresponding author: Jungho Im (ersgis@unist.ac.kr)

† These authors contributed equally: Siwoo Lee, Cheolhee Yoo

Abstract

Urban morphology and background climate are evolving drivers of the urban heat island (UHI) effect, yet the thermal influence of surrounding urban structure and its coupling with climate remain elusive. Here, we show that climate and morphology jointly shape global urban heat. Using a six-class urban typology, long-term climatology, and machine learning, we quantify the thermal influence of surrounding urban structure and project future urban heat across 2,213 cities. We define a city-level thermal impact of the surrounding built environment (T_{BE}) as the area-weighting UHI change induced by specific built-up types. Climatically, cold regions most frequently exhibit high daytime T_{BE}, while arid regions dominate high nighttime T_{BE}. Structurally, a universal pattern persists; high T_{BE} corresponds to denser and taller forms, whereas sparser and lower types dominate low T_{BE} during day and night. Future projections indicate that climate change dominates T_{BE} change in 69% of cities, whereas the Global South exhibits stronger tendencies toward morphology-driven and synergistic intensification than the Global North. Our results highlight the need for locally tailored adaptation strategies that target the dominant drivers—climatic, morphological, or both.

Introduction

Cities provide essential shelter and infrastructure but disrupt the surface energy balance through modifications in land cover and anthropogenic activities[1-2]. The resulting local temperature increase—the urban heat island (UHI) effect[3]—poses growing environmental and health risks, lengthening heatwaves and aggravating air pollution[4-6]. Yet, both the cause and magnitude of urban heating vary widely with local morphology[7-9], background climate[10-12], and time of day[13-14]. This complexity limits the ability to generalize across regions and complicates the design of effective adaptation strategies.

Urban morphology strongly influences local microclimates. Variations in building density, height, and material composition create marked inter- and intra- urban differences in thermal environment[15-16]. While many regional studies have sought to quantify the thermal effects of the surrounding built environment[16-18], most focus on narrow typologies or individual cities [16, 19-20], leaving the broader structural influence of diverse morphologies largely unexplored.

At the same time, background climate exerts a dominant control on surface energy fluxes through its effects on evapotranspiration and atmospheric convection[21-22]. Consequently, the magnitude and timing of the UHI vary among climate zones[23-25]. Previous large-scale analyses of the impact of background climate on UHI have two major limitations. Firstly, they have mostly been done based on satellite-derived land surface temperature (or surface UHI)[7, 11, 26], which can show large deviations from air temperature or canopy UHI[27-29], the latter being much more relevant for human systems. Secondly, previous studies have often examined a baseline climate state for present-day conditions[1, 11], without accounting for how urban areas and their background climate have evolved and will continue to change in the future. Even within a single climate regime, however, large differences persist[1-2, 30], implying that local morphological factors modulate the thermal response beyond the climatic baseline. Addressing this interplay is essential to identify the physical processes underlying urban heat and to develop transferable mitigation strategies. Furthermore, given the accelerating pace of urbanization and climate change[31-32], there is an urgent need to understand the combined effects of climate and urban morphology on the urban thermal environment.

This research gap is particularly relevant as cities continue to evolve[33]. Global-scale projections of how cities will respond to concurrent climate change and urban expansion remain scarce[34-36]. It is not yet clear whether future urban heat will be driven primarily by changes in background climate, by shifts in urban form, or by their combined effects. Because these sensitivities depend on regional development trajectories and adaptive capacities, they may produce systematically uneven urban heat burdens across global cities.

Here, we propose a unified workflow to disentangle and quantify the effects of climate and urban morphology on urban heat across 2,213 cities worldwide (Fig. 1; see Methods for details) using a machine learning framework that integrates canopy-level UHI intensity, built-up types, and long-term climatic variables. Using this framework, we define a new bulk factor, the thermal impact of the surrounding built environment (T_{BE}) to capture how combinations of local structures influence diurnal heat patterns across climate zones, thereby explaining the substantial intra-climate variability observed in cities. Finally, we evaluate how these combined drivers will shape future local urban warming across three Shared Socioeconomic Pathways (SSP), explicitly modeling the changing urban morphology within evolving boundaries from the past to the future. Using this approach, we examine how the effects of the climate and morphological drivers differ between cities in the Global South and the Global North. Understanding these patterns provides the foundation for more targeted and equitable approaches to urban heat mitigation. This integrated framework couples high-resolution morphological, climatic, and thermal data to isolate how surrounding structures influence local and city-scale heat. By combining empirical modeling with physically interpretable metrics, it enables cross-climate comparisons and scenario-based projections of how urban form and climate together will determine the future thermal landscape of global cities.

Results

Quantifying the thermal influence of surrounding structures across climate zones

By comparing UHI intensity across different surrounding urban morphology compositions, we derived the surrounding urban morphology-induced UHI change (ΔUHI) as a measure of the additional heating or cooling caused by nearby urban forms (see Methods for details). Surrounding urban morphology exerts a significant thermal influence on the central pixel, and the strength and direction of this influence vary with both morphology and climate (Fig. 2).

Clear structural gradients emerge across the six built-up types. High-density types consistently show larger ΔUHI than medium- and low-density forms. This density gradient becomes more pronounced at night, with mean ΔUHI declining from 0.44 ± 0.21 °C to 0.21 ± 0.12 °C across density classes during the day, and from 0.50 ± 0.15 °C to 0.18 ± 0.12 °C at night. Building height exerts an additional influence: high-rise forms generally exhibit larger ΔUHI than their low-rise counterparts. This contrast, primarily associated with building height, intensifies at night, with the average ΔUHI difference increasing from 0.06 °C during the day to 0.16 °C at night. These day–night contrasts suggest that the thermal influence of surrounding urban morphology is stronger at night, reflecting enhanced heat storage and delayed release in denser, taller urban forms.

Background climate further modulates ΔUHI. Daytime ΔUHI is smallest in arid regions (0.09 ± 0.04 °C) and stronger in cold (0.47 ± 0.14 °C), temperate (0.39 ± 0.14 °C), and tropical (0.38 ± 0.15 °C) climates (Fig. 2a). At night, the pattern reverses: arid regions exhibit the highest ΔUHI (0.43 ± 0.21 °C), followed by cold (0.40 ± 0.19 °C), temperate (0.34 ± 0.16 °C), and tropical (0.21 ± 0.12 °C) zones (Fig. 2b). Even within the same built-up type, ΔUHI differs overall significantly across climates ($P < 0.001$, two-way ANOVA), suggesting that even identical urban forms can exert quantitatively different thermal influences depending on the climatic background. The response to increasing surrounding urbanization also varies across climate zones, although clear structural gradients persist, highlighting the importance of both climate and urban morphology (Supplementary Fig. 1). These results quantify the structural contribution to urban heat beyond the scale of local case studies[16-18].

Climate and morphology jointly shape global diurnal urban heat

For each city, we computed the thermal impact of the surrounding built environment (T_{BE}) as the weighted sum of ΔUHI values according to the areal proportions of each built-up type (see Methods for details). T_{BE} expresses the integrated thermal influence of local morphology on urban heat. Mapping T_{BE} across 2,213 cities by day and night shows pronounced spatial heterogeneity and significant climatic differences (Fig. 3; $P < 0.05$, Kruskal–Wallis H test). Elevated daytime T_{BE} is distributed in a spatially heterogeneous and globally scattered pattern, with relatively high values in parts of Europe, northeastern North America, and East Asia. In contrast, minimal values dominate in arid regions such as the Middle East and western North America (see climate zones in Supplementary Fig. 2). At night, spatial patterns shift: elevated T_{BE} spreads across much of the Northern Hemisphere mid-latitudes (30–60°N), particularly the Middle East and western North America (Fig. 3c).

To allow comparison across climates, we divided cities into three T_{BE} categories using the Jenks natural breaks method[37]. Globally, 11.48% of cities fall in the high daytime T_{BE} category (> 0.41 °C). Among climate zones, the cold regime exhibits the largest share of high daytime T_{BE} cities (24.13%) (Fig. 3b and Supplementary Table 1). At night, 6.87% of all cities exhibit a high T_{BE} category (> 0.39 °C), with arid zones containing the largest share (10.67%) of these cases (Fig. 3d and Supplementary Table 1).

Within individual climate zones, variations in T_{BE} largely reflect differences in structure. In arid zones, for example, daytime ΔUHI is weakest overall, yet about 5% of arid cities still reach high T_{BE} values (Fig. 2a and 3b). Comparing urban morphology compositions reveals systematic contrasts (Fig. 3e, f): cities with high daytime T_{BE} have greater fractions of high-density high-rise (2.43–4.75%) or medium-density high-rise types (2.36–7.01%). Cities with low daytime T_{BE} (≤ 0.14 °C) show reduced coverage of these forms and generally higher shares of low-density low-rise type (53.04–66.89%). At night, the same morphological tendencies persist, augmented by larger proportions of higher-density and high-rise forms in high T_{BE} cities (Fig. 3f). Because structural inventories are broadly similar among climate zones (Supplementary Fig. 3), these internal composition differences explain why cities within the same climate can display markedly different thermal signatures: local morphology and regional climate act together to determine T_{BE}.

Regional disparities in future urban heat under climate and morphology change

We project future T_{BE} by combining climate and morphology scenarios (SSP1, SSP2, SSP5). Under SSP5 (shown), most cities are projected to experience an increase in T_{BE} relative to the present, although both the magnitude and direction of change vary (Fig. 4a, b). During the day, pronounced increases are concentrated in India and northeastern North America, whereas decreases are more common in the Middle East and western North America. At night, T_{BE} intensification becomes more widespread, with particularly strong increases across Europe, Africa, and China. This diversity in T_{BE} change reflects differing balances between the dominant driver of change and the synergistic effect arising from the combined influence of climate change and urban morphology.

Climate change is the dominant driver of future daytime T_{BE} change in 1,531 cities (69%) and nighttime T_{BE} change in 1,517 cities (69%), exceeding the contribution of morphological change (Fig. 4c, d). Around 10% of cities are classified as comparable, indicating similar magnitudes of the climate-only and morphology-only contributions. Although minimal effects—

indicating little additional warming or cooling from interactions between climate change and morphological change—are the most widespread during both the day (38%) and at night (43%), considerable synergistic warming remains common, occurring in 34% of cities globally (Fig. 4e, f). Notably, both dominant drivers and synergistic effects vary substantially among cities within the same country, highlighting marked heterogeneity in future T_{BE} responses. This heterogeneity among cities provides a fundamental basis for the dominant factor in future T_{BE} and underscores the need to tailor adaptation measures to local conditions.

A broad Global South–North asymmetry is evident in the distribution of dominant drivers and synergistic effects. During the day, a larger share of Global South cities exhibits morphology-dominant T_{BE} increases (24.4%) than Global North cities (12.0%; Fig. 4g). By contrast, more than half of Global North cities (60.2%) show climate-dominant T_{BE} increases. This asymmetry is not limited to the dominant factor. It is also apparent in the synergistic effect, with the Global South consistently showing stronger tendencies toward warming than the Global North, as also noted in previous research[38]. A similar asymmetry is observed at night (Fig. 4i, g). These patterns persist across SSPs and are strongest under SSP5 (Supplementary Figs. 4–5). Together, the results argue for region-specific adaptation that accounts for the dominant driver—climate, morphology, or both—in each city.

Discussion

Growing concerns over climate change and rapid urbanization have brought renewed attention to the thermal consequences of city growth. Previous studies have identified climate and morphology as primary factors shaping the urban thermal environment[11, 16, 19, 39], but quantitative assessments of how surrounding urban structures contribute to local heat remain largely unknown. Even fewer investigations have considered the combined influence of climate and urban form or projected their joint impacts on a global scale. By explicitly linking UHI intensity to the composition of surrounding built-up types across 2,213 cities, this study provides a consistent quantification of this structural thermal influence and reveals how morphology and background climate interact to determine present and future urban heat.

The global contrasts observed here highlight that broad climatic regimes set the background for local heating. Arid cities show relatively weak daytime but strong nighttime thermal impact, a pattern consistent with limited evaporative cooling and high sensible-heat storage[11, 40]. The subsequent release of stored energy intensifies nocturnal heat[41]. Vegetation height, which increases with precipitation[42], also modifies roughness and convective efficiency. In arid regions, urban surfaces can be aerodynamically rougher than surrounding landscapes, enhancing daytime convective mixing and contributing to a distinct daytime thermal response[1, 27]. In humid climates, by contrast, more densely vegetated rural surfaces often exchange heat more efficiently than dense urban forms[11]. Structural characteristics further explain large intra-climate differences. Denser- and higher forms restrict ventilation and trap radiation, amplifying daytime heat[2, 19]. At night, energy accumulated in dense materials sustains warmth, strengthening the structural gradient relative to daytime[2]. These processes explain the pronounced climatic and structural signatures observed during both the day and at night.

Future projections show climate change dominates T_{BE} changes in most cities, while morphological change continues to modulate urban heat through frequent synergistic warming and strong inter-city variability. A broad socioeconomic asymmetry is also evident. Cities in the

Global South more often show stronger contributions from morphological change and its interaction with climate change, whereas climatic signal more frequently dominates in the Global North. This asymmetry reflects divergent development pathways, with generally mature, slower-growing cities in the North contrasting with the more rapid expansion in the South[31, 38, 43]. Similar patterns are also observed across income groups (Supplementary Fig. 6), with climate-dominant responses more common in high-income cities and morphology-related contributions more pronounced in lower-middle-income cities. These patterns suggest that the observed asymmetry is not solely an artefact of the Global South–North classification.

However, not all cities warm uniformly. A significant fraction exhibits future T_{BE} mitigation, consistent with observed heterogeneous UHI trends[44-45]. SHAP analysis further supports this interpretation by showing that background climate acts as a nonlinear and climate-dependent modifier of urban heat (Supplementary Fig. 7). Response curves for climate variables frequently show inflection points, slope reversals, or response flattening, indicating that their thermal contributions shift across climatic conditions rather than increasing or decreasing monotonically[11, 24]. Similar patterns have also been reported in previous studies. Precipitation shows the clearest climate-specific contrast, with stronger negative nighttime contributions in wetter tropical, temperate, and cold climates, but weaker and more distinct responses in arid cities. These patterns are consistent with the key role of moisture availability and associated shifts in surface-energy partitioning in urban–rural thermal contrasts[1, 11]. Recognizing such nonlinear, regime-dependent responses is essential for anticipating shifts in local urban heat regimes and for designing adaptive strategies.

More broadly, the proposed metrics ΔUHI and T_{BE} provide an interpretable framework for quantifying how surrounding urban morphology and background climate jointly shape urban heat from the neighborhood to the city scale. Because urban structures are intentionally spatially organized rather than randomly distributed[46–47], ΔUHI can inform urban development and heat-mitigation strategies by indicating which surrounding built types are associated with greater local warming or cooling effects across climatic regimes. Comparison with the randomly mixed baseline further clarifies whether local heat amplification is driven primarily by the amount of surrounding urbanization or by the spatial clustering of similar built types (Supplementary Fig. 8). Building on these neighborhood-scale insights, T_{BE} identifies the dominant drivers and synergistic effects governing each city's thermal regime, thereby providing a basis for targeted adaptation. In morphology-dominated cities, revising density, height, and surface materials may yield the largest benefit, whereas in climate-dominated regions, vegetation and evapotranspiration enhancement could be more effective. This heterogeneity underscores that effective heat mitigation requires moving beyond a one-size-fits-all approach toward locally tailored strategies that target each city’s primary thermal driver. In this context, our framework should be understood as a model-derived diagnostic for comparative attribution rather than a directly measurable temperature change.

Several uncertainties remain. Our findings are based on annual mean maximum (daytime) and minimum (nighttime) temperature conditions rather than season-specific extremes, providing a globally comparable baseline but potentially smoothing seasonal mechanisms. Supplementary summer analyses nevertheless show that the main climate- and morphology-dependent patterns remain robust, although the absolute magnitudes of the proposed metrices are generally larger in summer (Supplementary Figs. 9–11). Our analysis captures structural composition but not explicitly resolve spatial configuration, which influences radiative trapping and airflow[48-49]. Moreover, spatial heterogeneity in built-surface materials and their thermal properties, together with SSP-specific differences in future horizontal urban expansion, is not explicitly represented because of limited global data availability. Finally, our analysis uses a single definition of urban areas, which would impact some of the quantitative results we present here. Note that the climate dependence of the UHI effect has been qualitatively seen across different urban representations from various global datasets[50]. Future work should extend this framework to season-specific conditions, incorporate configuration-sensitive metrics, and develop more comprehensive scenario-dependent representations of urban morphology and surface properties. Another priority will be to link these thermal effects to coupled impacts on air quality, energy demand, and environmental health[6, 51–52], enabling a more integrated assessment of climate-sensitive urban risk.

Overall, these results show that urban heat is a product of the coupled dynamics of climate and morphology rather than either factor alone. By identifying the physical and structural determinants of local urban warming, this study provides a quantitative basis for designing cities that remain livable and resilient in a warming world.

Methods

Study area and data

We used the Global Human Settlement Urban Centre Database[53] to analyze global urban thermal environments. Of the 11,351 urban areas delineated for 2020, we selected 2,213 cities with extents greater than 50 km² (Supplementary Fig. 2) based on data completeness and compatibility with the other dataset used in this study. These cities span four Köppen-Geiger climate zones[54]: 430 arid, 549 tropical, 946 temperate, and 315 cold. The sample comprises 739 cities in the Global South and 1,474 in the Global North, following the classification of the Finance Center for South-South Cooperation[55].

Urban typology. We classified urban areas into six three-dimensional (3D) urban form types based on building density and height, using a modified classification scheme adapted from the local climate zone framework[3, 56–57]. A conceptual schematic of the six urban form types is provided in Supplementary Fig. 12. The horizontal dimension was characterized using the Global Human Settlement Layer (GHSL) built-up surface dataset, which quantifies the amount of built-up surface per 1 km pixel[58] and was grouped into three classes: low (<15% of built-up surface), medium (15–30%), and high (≥30%). Pixels with built-up surface below 2% were treated as non-built-up. For the vertical dimension, we used FU3D, a global projection dataset of future urban 3D expansion[59], and defined a height proxy as the ratio of building volume to GHSL built-up surface. This proxy was classified into two levels: low-rise (<10 m) and high-rise (≥10 m). We adopted this approach because the FU3D height product represents a flattened, pixel-averaged height over the entire 1 km pixel[59], which can smooth vertical variation in partially built-up pixels. Relating building volume to GHSL built-up surface better captures the effective vertical intensity of urban form for classification (Supplementary Fig. 13).

The same six-class typology was applied to both present and future urban morphology. For the present-day analysis, we used the 2020 GHSL built-up surface and FU3D building volume datasets under SSP2 (middle of the road). For future morphology, we integrated the 2050 GHSL built-up surface projection with three distinct SSP-specific FU3D building volume scenarios (SSP1, sustainability; SSP2, middle of the road; and SSP5, fossil-fueled development). This enabled morphological transitions across 2,213 global cities, driven by demographic and economic growth, to be characterized in terms of both horizontal expansion and vertical intensification (Supplementary Fig. 14).

Air temperature. Near-surface air temperature (SAT) was obtained from a global 1 km daily dataset[60] that integrates ground observations satellite-derived land surface temperature, and digital elevation model (DEM) data using spatially varying coefficient model. We extracted the 2020 records to maintain temporal consistency with the other datasets. From the daily SAT dataset, we calculated the annual mean of daily maximum temperature, which reflects peak daytime heat exposure during periods of intense human activity[29, 61–62], and the annual mean of daily minimum temperature, which captures nocturnal heat retention and cumulative overnight thermal stress under intensified nighttime UHI conditions[27, 63–64]. These variables were then used as indicators of daytime and nighttime thermal conditions, respectively.

Annual mean conditions were used in the main analysis to provide a stable, globally comparable baseline across cities in multiple climate zones and both hemispheres. To assess seasonal sensitivity, we further extracted local summer conditions, defined as June–August for the Northern Hemisphere and December–February for the Southern Hemisphere[25, 39].

Topographical data. Elevation data were taken from the Global Multi-resolution Terrain Elevation Data 2010 (GMTED2010), produced by the U.S. Geological Survey and the National Geospatial-Intelligence Agency. The 1 km product provides consistent topographic information globally, harmonized with other datasets.

Climatology. Current (1991-2020) and future (2041-2070) climate variables were obtained from high resolution (0.01°, ~ 1 km) gridded datasets[54]. The current climatology is based on an ensemble of observation-derived, high-resolution datasets. Future projections for SSP1-2.6, SSP2-4.5, and SSP5-8.5 represent the multi-model ensemble mean of a screened subset of 42 Coupled Model Intercomparison Project Phase 6 models. For consistency with the FU3D scenario nomenclature, these scenarios are hereafter referred to as SSP1, SSP2, and SSP5, respectively. All projections were statistically downscaled and bias-corrected using observed climatological conditions. Annual mean air temperature and total precipitation were calculated from monthly data.

Integrated framework

Local urban thermal conditions arise from background climate, which governs potential evapotranspiration and convective cooling[1, 11, 39], and from morphology, which modulates microclimates[15, 65], driving both inter- and intra-urban variability in UHI effects[7, 66]. We tested three hypotheses:

1) **Local influence**. UHI intensity depends on the characteristics of surrounding structures.

2) **Climatic modulation**. Climate alters the magnitude and direction of structures-induced thermal effects across zones and between day and night.

3) **Combined effects**. The joint impact of climate and morphology varies regionally, leading to heterogeneous thermal outcomes under future scenarios.

To evaluate these, we developed a global analytical framework combining SAT, urban morphology, and climatic variables (Fig. 1). Machine learning analysis captured interactions between morphology and climate, quantifying their joint effects on UHI and their sensitivity to changing conditions.

Pixel-based UHI intensity. UHI intensity is generally defined as the average temperature difference between urban and rural areas[25–27]. Here, we adapted this concept to the pixel-level, defining UHI intensity for each urban pixel relative to the mean temperature of rural reference pixels classified as non-built-up (built-up surface < 2%). Adaptive buffer zones were delineated around each city to ensure sufficient reference pixels, with buffer distance:

$$D_{buffer} = \left(\sqrt{2} - 1\right)\sqrt{\frac{C}{\pi}} \tag{1}$$

where D_{buffer} represents the buffer distance applied around each city, and C is city area (km^2). Reference pixels with elevations differing by more than ±50 meters from the city mean, or lacking valid SAT values (for example, water bodies or missing data) were excluded. Pixel-wise UHI intensity was then calculated separately for daytime and nighttime as:

$$\mathrm{UHI\ intensity}_i = \mathrm{SAT}(\mathrm{Urban}_i) - \overline{\mathrm{SAT}}(\mathrm{Non-built-up}) \tag{2}$$

where $\mathrm{UHI\ intensity}_i$ denotes the pixel-specific canopy urban heat island intensity, $\mathrm{SAT}(\mathrm{Urban}_i)$ indicates the near-surface air temperature of built-up pixel i of an individual city, and $\overline{\mathrm{SAT}}(\mathrm{Non-built-up})$ refers to the average near-surface air temperature of non-built-up pixels within corresponding urban boundary. This method represents an extension of the Simplified

Urban Extent (SUE) algorithm for calculating the UHI originally developed using broader land cover classes[39].

Spatial extent of surrounding thermal impact. To capture localized thermal interactions, we restrict the analysis to the eight immediate neighbors surrounding each central pixel (3×3 window). This spatial extent was chosen to represent the most immediate neighborhood context[2, 67], whereas larger windows are more likely to blend immediate neighborhood effects with broader contextual influences[68–69]. Consistent with this rationale, our empirical sensitivity analysis showed that larger spatial windows yielded only marginal improvements in model performance (Supplementary Table 2). We therefore adopt the 3 × 3 window as the primary analysis scale.

Machine learning model. We used eXtreme Gradient Boosting (XGBoost)[70] to model UHI intensity as a function of surrounding structure and environment. XGBoost is a tree-ensemble algorithm capable of representing nonlinear relationships and has been widely applied to environmental prediction[71–73].

Inputs included: (i) the proportion of each of six built-up types and non-built-up pixels within the eight neighboring pixels; (ii) mean and standard deviation of annual air temperature and precipitation at the center pixel; (iii) elevation of the center pixel; and (iv) the built-up type of the center pixel.

The target variable is pixel-level UHI intensity (Eq. 2). Separate models are trained for daytime and nighttime conditions. To mitigate the influence of spatial autocorrelation on model evaluation, we implemented a spatial block split by grouping samples into non-overlapping 10-km blocks. Blocked validation is preferable to random splitting when dependence structures are present because random splits can yield overoptimistic performance estimates. In contrast, spatially structured splits provide a more realistic assessment of performance on spatially unseen data[74–75]. These spatial blocks were then assigned to training (70%), validation (10%), and independent testing (20%) sets.

The 10-km block size was selected from an empirical distance-decay analysis of the target variable based on pairwise correlations computed across 1-km distance bins. Specifically, for each city, we quantified the correlation in pixel-level UHI intensity between randomly sampled pairs of pixels as a function of spatial separation. We defined the decorrelation distance as the first distance bin at which the absolute correlation fell below 0.05. This analysis yielded a median decorrelation distance of approximately 7.5 km across cities (Supplementary Fig. 15). Although this spatial block split provides a more stringent evaluation than a random split, it does not fully establish geographic transferability to entirely unseen regions. Given that the primary objective of our modelling framework is explanatory attribution rather than transfer predictions across regions, this evaluation design is appropriate for the scope of this study.

Model implementation was performed using the xgboost library, and hyperparameters, including the maximum tree depth (max_depth), learning rate (learning_rate), and number of estimators (n_estimators), were optimized using the optuna framework. To interpret feature contributions, we employed SHapley Additive exPlanations (SHAP)[76–77], which decomposes each prediction into additive effects of individual inputs. Positive SHAP values indicate a feature increases UHI relative to the mean prediction; negative values indicate a cooling influence.

Model simulations

We conducted model-based simulations using the trained XGBoost models to isolate the effects of surrounding structures. High model accuracy ($r > 0.8$; Supplementary Fig. 16) and close agreement between predicted and observed patterns (Supplementary Fig. 17) validate the approach.

Thermal influence of surrounding structures. The surrounding urban morphology-induced UHI change (ΔUHI) represents the additional heating or cooling attributable to the adjacent urban morphology relative to non-built-up surroundings. To isolate this effect, for each central built-up type, we define a baseline case ($S = 0$) in which a central built-up pixel is entirely surrounded by non-built-up pixels, representing the absence of surrounding structural influence. The comparison case ($S = 8$) assumes that all eight neighboring pixels are occupied by a single built-up type. Because urban structures are typically spatially organized rather than randomly distributed[46–47], these idealized scenarios were used to isolate the maximum specific thermal influence of surrounding urban morphology. Accordingly, the main ΔUHI metric for the surrounding built type i is calculated as:

$$\Delta\text{UHI}_m = \text{UHI intensity}_{c,m}(S = 8) - \text{UHI intensity}_c(S = 0) \quad (3)$$

where $\text{UHI intensity}_{c,m}(S = 8)$ denotes the canopy urban heat island intensity at the central pixel when all eight surrounding pixels are occupied by specific built-up type m, and $\text{UHI intensity}_\text{c}(S = 0)$ denotes the canopy urban heat island intensity at the same central pixel when all eight surrounding pixels are non-built-up areas. This analysis was repeated separately for each central built-up type to account for differences in sensitivity to surrounding morphology. Future ΔUHI was estimated using the same formulation with future climatic inputs.

To complement this primary analysis and provide additional interpretive context, we further evaluate transitional scenarios in which the number of surrounding pixels occupied by built-up type m increased progressively from one to eight:

$$\Delta\mathrm{UHI}_m(S) = \mathrm{UHI\ intensity}_{c,m}(S) - \mathrm{UHI\ intensity}_c(S = 0), \qquad S \in \{1, \dots, 8\} \tag{4}$$

where $\Delta\mathrm{UHI}_m(S)$ denotes the change in canopy urban heat island intensity associated with S surrounding pixels of built-up type m. By varying S, we can characterize the thermal gradient as the local neighborhood transitions from a fully non-built-up state to a fully urbanized environment. Furthermore, to provide a mixed-composition baseline, we computed the mean predicted UHI intensity across all feasible neighborhood compositions of the eight surrounding pixels ($N = 3{,}003$; corresponding to six built-up types and one non-built-up):

$$\mathrm{UHI}_c^{mix} = \frac{1}{N}\sum_{j=1}^{N} \mathrm{UHI}_{c,j} \tag{5}$$

where $\mathrm{UHI}_{c,j}$ denotes the predicted canopy urban heat island intensity for the j-th neighborhood composition. This baseline represents the expected thermal response under mixed neighborhood conditions. Comparing the homogeneous case ($S = 8$) with this mixed-composition baseline provides additional context for the effect associated with local clustering of similar urban morphology.

Thermal impact of surrounding built environment. To quantify the city-scale thermal influence of urban morphological composition, we define the thermal impact of the surrounding built environment (T_{BE}) as an integrative comparative index for attribution across cities under current and future scenarios. Here, T_{BE} represents a model-derived measure of thermal influence of the built environment—particularly the contributions of building height and density—as mediated by background climatic conditions. It is therefore intended as a comparative index rather than a directly measurable temperature change. Specifically, T_{BE} is calculated as the area-weighted sum of ΔUHI, normalized by the total buffered urban area of each city:

$$T_{BE} = \sum_{m=1}^{6} (\Delta\mathrm{UHI}_m \times \frac{\mathrm{Area}_m}{\mathrm{Area}_{\mathrm{urb}}} \tag{6}$$

where $\Delta\mathrm{UHI}_m$ indicates the surrounding urban morphology-induced UHI change associated with built-up type m, Area_m is the area of built-up type m, and $\mathrm{Area}_{\mathrm{urb}}$ is the total buffered urban area. This calculation is performed independently for each city. For future scenario, $\Delta\mathrm{UHI}_m$ and Area_m are updated to reflect climate change and urban growth, allowing T_{BE} to capture scenario-dependent changes in the thermal influence of the built environment as cities expand.

Data availability

The datasets in this study are publicly available as follows or can be obtained from Google Earth Engine. Global Human Settlement Urban Center Database and GHSL built-up surface datasets are available at https://human-settlement.emergency.copernicus.eu/index.php. Near-surface air temperature data are available at https://gee-community-catalog.org/projects/airtemp/ (ref. 60). GMTED2010 is available at https://earthexplorer.usgs.gov/. The dataset of Köppen-Geiger climate zones and climatology can be accessed at https://www.gloh2o.org/koppen/ (ref. 54). The dataset of FU3D can be obtained from https://doi.org/10.6084/m9.figshare.26795932 (ref. 59). The data generated in this study are provided in the Source data file.

Code availability

The code developed in this study is publicly available at the following GitHub repository: https://github.com/siwoolee-code/Climorph.

References

1. Zhao, L., Lee, X., Smith, R. B. & Oleson, K. Strong contributions of local background climate to urban heat islands. *Nature* **511**, 216–219 (2014).
2. Li, Y., Schubert, S., Kropp, J. P. & Rybski, D. On the influence of density and morphology on the urban heat island intensity. *Nat. Commun.* **11**, 2647 (2020).
3. Stewart, I. D. & Oke, T. R. Local climate zones for urban temperature studies. *Bull. Amer. Meteorol. Soc.* **93**, 1879–1900 (2012).
4. Voogt, J. A. & Oke, T. R. Thermal remote sensing of urban climates. *Remote Sens. Environ.* **86**, 370–384 (2003).
5. Sharma, R., Hooyberghs, H., Lauwaet, D. & De Ridder, K. Urban heat island and future climate change—implications for Delhi's heat. *J. Urban Health* **96**, 235–251 (2019).
6. Li, H. et al. Interaction between urban heat island and urban pollution island during summer in Berlin. *Sci. Total Environ.* **636**, 818–828 (2018).
7. Bechtel, B. et al. SUHI analysis using Local Climate Zones—a comparison of 50 cities. *Urban Clim.* **28**, 100451 (2019).

8. Lee, S. et al. A hybrid machine learning approach to investigate the changing urban thermal environment by dynamic land cover transformation: a case study of Suwon, Republic of Korea. *Int. J. Appl. Earth Obs. Geoinf.* **122**, 103408 (2023).
9. Liu, Y. et al. Urban heat island effects of various urban morphologies under regional climate conditions. *Sci. Total Environ.* **743**, 140589 (2020).
10. Liu, Z. et al. Surface warming in global cities is substantially more rapid than in rural background areas. *Commun. Earth Environ.* **3**, 219 (2022).
11. Manoli, G. et al. Magnitude of urban heat islands largely explained by climate and population. *Nature* **573**, 55–60 (2019).
12. Deng, H., Feng, J., Liu, K., Xiong, Y. & Cao, J. Local climate zone framework: seasonal dynamics of surface urban heat island and its influencing factors in three Chinese urban agglomerations. *GIScience Remote Sens.* **62**, 2490317 (2025).
13. Jiang, S. et al. Surface air temperature differences of intra-and inter-local climate zones across diverse timescales and climates. *Build. Environ.* **222**, 109396 (2022).
14. Kim, J., Sohn, S., Wang, Z. & Kim, Y. Nonuniform response of vegetation phenology to daytime and nighttime warming in urban areas. *Commun. Earth Environ.* **5**, 308 (2024).
15. Middel, A., Häb, K., Brazel, A. J., Martin, C. A. & Guhathakurta, S. Impact of urban form and design on mid-afternoon microclimate in Phoenix Local Climate Zones. *Landsc. Urban Plan.* **122**, 16–28 (2014).
16. Nugroho, N. Y., Triyadi, S. & Wonorahardjo, S. Effect of high-rise buildings on the surrounding thermal environment. *Build. Environ.* **207**, 108393 (2022).
17. Li, H. et al. Quantifying urban heat island intensity and its physical mechanism using WRF/UCM. *Sci. Total Environ.* **650**, 3110–3119 (2019).

18. Van Hove, L. W. A. et al. Temporal and spatial variability of urban heat island and thermal comfort within the Rotterdam agglomeration. *Build. Environ.* **83**, 91–103 (2015).
19. He, B. J., Ding, L. & Prasad, D. Relationships among local-scale urban morphology, urban ventilation, urban heat island and outdoor thermal comfort under sea breeze influence. *Sustain. Cities Soc.* **60**, 102289 (2020).
20. Yang, X. & Li, Y. The impact of building density and building height heterogeneity on average urban albedo and street surface temperature. *Build. Environ.* **90**, 146–156 (2015).
21. Zhang, K. et al. Increased heat risk in wet climate induced by urban humid heat. *Nature* **617**, 738–742 (2023).
22. Park, K., Baik, J. J., Jin, H. G. & Tabassum, A. Changes in urban heat island intensity with background temperature and humidity and their associations with near-surface thermodynamic processes. *Urban Clim.* **58**, 102191 (2024).
23. Eldesoky, A. H., Gil, J. & Pont, M. B. The suitability of the urban local climate zone classification scheme for surface temperature studies in distinct macroclimate regions. *Urban Clim.* **37**, 100823 (2021).
24. Yang, L. et al. Different explanations for surface and canopy urban heat island effects in relation to background climate. *iScience* **27**, 109154 (2024).
25. Du, H. et al. Simultaneous investigation of surface and canopy urban heat islands over global cities. *ISPRS J. Photogramm. Remote Sens.* **181**, 67–83 (2021).
26. Kim, Y., Yoo, C. & Im, J. Nighttime satellite land surface temperature for urban applications: achievements, challenges, and future prospects. *GIScience Remote Sens.* **62**, 2527990 (2025).
27. Venter, Z. S., Chakraborty, T. & Lee, X. Crowdsourced air temperatures contrast satellite measures of the urban heat island and its mechanisms. *Sci. Adv.* **7**, eabb9569 (2021).

28. Chakraborty, T., Venter, Z. S., Qian, Y. & Lee, X. Lower urban humidity moderates outdoor heat stress. *AGU Adv.* **3**, e2022AV000729 (2022).
29. Yoo, C. et al. Diurnal urban heat risk assessment using extreme air temperatures and real-time population data in Seoul. *iScience* **26**, 108151 (2023).
30. Yuan, B. et al. Global distinct variations of surface urban heat islands in inter-and intra-cities revealed by local climate zones and seamless daily land surface temperature data. *ISPRS J. Photogramm. Remote Sens.* **204**, 1–14 (2023).
31. United Nations, Department of Economic and Social Affairs, Population Division. World Urbanization Prospects: The 2018 Revision (ST/ESA/SER.A/420) (United Nations, 2019).
32. Intergovernmental Panel on Climate Change. *Climate Change 2021: The Physical Science Basis* (Cambridge Univ. Press, 2021).
33. Chakraborty, T. C. & Qian, Y. Urbanization exacerbates continental-to regional-scale warming. *One Earth* **7**, 1387–1401 (2024).
34. Sachindra, D. A., Ng, A. W. M., Muthukumaran, S. & Perera, B. J. C. Impact of climate change on urban heat island effect and extreme temperatures: a case-study. *Q. J. R. Meteorol. Soc.* **142**, 172–186 (2016).
35. Lauwaet, D. et al. Assessing the current and future urban heat island of Brussels. *Urban Clim.* **15**, 1–15 (2016).
36. Huang, K., Li, X., Liu, X. & Seto, K. C. Projecting global urban land expansion and heat island intensification through 2050. *Environ. Res. Lett.* **14**, 114037 (2019).
37. Jenks, G. F. The data model concept in statistical mapping. *Int. Yearb. Cartogr.* **7**, 186–190 (1967).

38. Du, H. et al. Exacerbated heat stress induced by urban browning in the Global South. *Nat. Cities* **2**, 157–169 (2025).
39. Chakraborty, T. & Lee, X. A simplified urban-extent algorithm to characterize surface urban heat islands on a global scale and examine vegetation control on their spatiotemporal variability. *Int. J. Appl. Earth Obs. Geoinf.* **74**, 269–280 (2019).
40. Oke, T. R. *Boundary Layer Climates* (Routledge, 2002).
41. Fitria, R., Kim, D., Baik, J. & Choi, M. Impact of biophysical mechanisms on urban heat island associated with climate variation and urban morphology. *Sci. Rep.* **9**, 19503 (2019).
42. Ehbrecht, M. et al. Global patterns and climatic controls of forest structural complexity. *Nat. Commun.* **12**, 519 (2021).
43. Zhang, Y. et al. A global North-South division line for portraying urban development. *iScience* **24**, 102744 (2021).
44. Scott, A. A., Waugh, D. W. & Zaitchik, B. F. Reduced urban heat island intensity under warmer conditions. *Environ. Res. Lett.* **13**, 064003 (2018).
45. Yang, Q. et al. A global urban heat island intensity dataset: generation, comparison, and analysis. *Remote Sens. Environ.* **312**, 114343 (2024).
46. Anas, A., Arnott, R. & Small, K. A. Urban spatial structure. *J. Econ. Lit.* **36**, 1426–1464 (1998).
47. Batty, M. The size, scale, and shape of cities. *Science* **319**, 769–771 (2008).
48. Gustafson, E. J. Quantifying landscape spatial pattern: what is the state of the art? *Ecosystems* **1**, 143–156 (1998).

49. Zhou, W., Huang, G. & Cadenasso, M. L. Does spatial configuration matter? Understanding the effects of land cover pattern on land surface temperature in urban landscapes. *Landsc. Urban Plan.* **102**, 54–63 (2011).
50. Chakraborty, T. C. et al. Large disagreements in estimates of urban land across scales and their implications. *Nat. Commun.* **15**, 9165 (2024).
51. Akbari, H., Pomerantz, M. & Taha, H. Cool surfaces and shade trees to reduce energy use and improve air quality in urban areas. *Solar Energy* **70**, 295–310 (2001).
52. Li, X. et al. Urban heat island impacts on building energy consumption: a review of approaches and findings. *Energy* **174**, 407–419 (2019).
53. Melchiorri, M. et al. *Stats in the City–the GHSL Urban Centre Database 2025* (European Commission, 2024).
54. Beck, H. E. et al. High-resolution (1 km) Köppen-Geiger maps for 1901–2099 based on constrained CMIP6 projections. *Sci. Data* **10**, 724 (2023).
55. Finance Center for South-South Cooperation. Global South countries. http://www.fc-ssc.org/en/partnership_program/south_south_countries.
56. Chen, T. H. K. et al. Mapping horizontal and vertical urban densification in Denmark with Landsat time-series from 1985 to 2018: a semantic segmentation solution. *Remote Sens. Environ.* **251**, 112096 (2020).
57. Chen, T. H. K. et al. Higher depression risks in medium-than in high-density urban form across Denmark. *Sci. Adv.* **9**, eadf3760 (2023).
58. Schiavina, M. et al. *GHSL WUP Projections Data Package 2025* (European Commission, 2025).

59. Zhao, Q., Meng, Q., Gao, L. & Zhu, M. FU3D: the first global projections of future urban three-dimensional (3D) expansion for the 21st century under shared socioeconomic pathways. *Sci. Data* **12**, 1555 (2025).
60. Zhang, T. et al. A global dataset of daily near-surface air temperature at 1-km resolution (2003–2020). *Earth Syst. Sci. Data* **14**, 1–18 (2022).
61. Lee, S. et al. Mapping nationwide 1 km hourly human mobility (2022–2024) across South Korea using multi-source data. *GIScience Remote Sens.* **63**, 2633052 (2026).
62. Bergroth, C., Järv, O., Tenkanen, H., Manninen, M. & Toivonen, T. A 24-hour population distribution dataset based on mobile phone data from Helsinki Metropolitan Area, Finland. *Sci. Data* **9**, 39 (2022).
63. He, C. et al. The effects of night-time warming on mortality burden under future climate change scenarios: a modelling study. *Lancet Planet. Health* **6**, e648–e657 (2022).
64. Basu, R. High ambient temperature and mortality: a review of epidemiologic studies from 2001 to 2008. *Environ. Health* **8**, 40 (2009).
65. Kamal, A. et al. Impact of urban morphology on urban microclimate and building energy loads. *Energy Build.* **253**, 111499 (2021).
66. Mentaschi, L. et al. Global long-term mapping of surface temperature shows intensified intra-city urban heat island extremes. *Global Environ. Change* **72**, 102441 (2022).
67. Tobler, W. R. A computer movie simulating urban growth in the Detroit region. *Econ. Geogr.* **46**, 234–240 (1970).
68. Shi, Y. et al. Influence of landscape features on urban land surface temperature: scale and neighborhood effects. *Sci. Total Environ.* **771**, 145381 (2021).

69. Li, X. & Zhou, W. Optimizing urban greenspace spatial pattern to mitigate urban heat island effects: extending understanding from local to the city scale. *Urban For. Urban Green.* **41**, 255–263 (2019).

70. Chen, T. & Guestrin, C. XGBoost: a scalable tree boosting system. *Proc. 22nd ACM SIGKDD Int. Conf. Knowl. Discov. Data Min.* 785–794 (2016).

71. Lee, Y., Son, B., Im, J., Zhen, Z. & Quackenbush, L. J. Two-step carbon storage estimation in urban human settlements using airborne LiDAR and Sentinel-2 data based on machine learning. *Urban For. Urban Green.* **94**, 128239 (2024).

72. Yi, Z. et al. Decoding urban emissions: the overlooked impact of commercial and public service zones across regions and seasons. *GIScience Remote Sens.* **62**, 2492971 (2025).

73. Sun, H. et al. Agricultural drought dynamics in China during 1982–2020: a depiction with satellite remotely sensed soil moisture. *GIScience Remote Sens.* **60**, 2257469 (2023).

74. Ploton, P. et al. Spatial validation reveals poor predictive performance of large-scale ecological mapping models. *Nat. Commun.* **11**, 4540 (2020).

75. Roberts, D. R. et al. Cross-validation strategies for data with temporal, spatial, hierarchical, or phylogenetic structure. *Ecography* **40**, 913–929 (2017).

76. Lundberg, S. M. & Lee, S. I. A unified approach to interpreting model predictions. *Adv. Neural Inf. Process. Syst.* **30**, (2017).

77. Kang, E. et al. An explainable AI framework for spatiotemporal risk factor analysis in public health: a case study of cardiovascular mortality in South Korea. *GIScience Remote Sens.* **61**, 2436997 (2024).

Funding

This work was supported by the National Research Foundation of Korea (NRF) Grant through the Ministry of Science and Information and Communication Technology (MSIT) (No. NRF-2021R1A2C2008561 and RS-2025-02310080). T.C. was supported by the Earth and Environmental Systems Modeling program area of the U.S. Department of Energy (DOE) Office of Science's Biological and Environmental Research program through a DOE Early Career Award. Pacific Northwest National Laboratory is operated for the DOE by the Battelle Memorial Institute under contract DE-AC05-76RL01830.

Author contributions

S.L. and C.Y. designed the research, performed the modeling and data analysis, and led the manuscript writing. B.S., D.C., TC, and J.I. contributed to the discussion of ideas, interpretation of results, and revision of the manuscript. J.I. supervised the project and contributed to the research design.

Competing interests

The authors declare no competing interests.

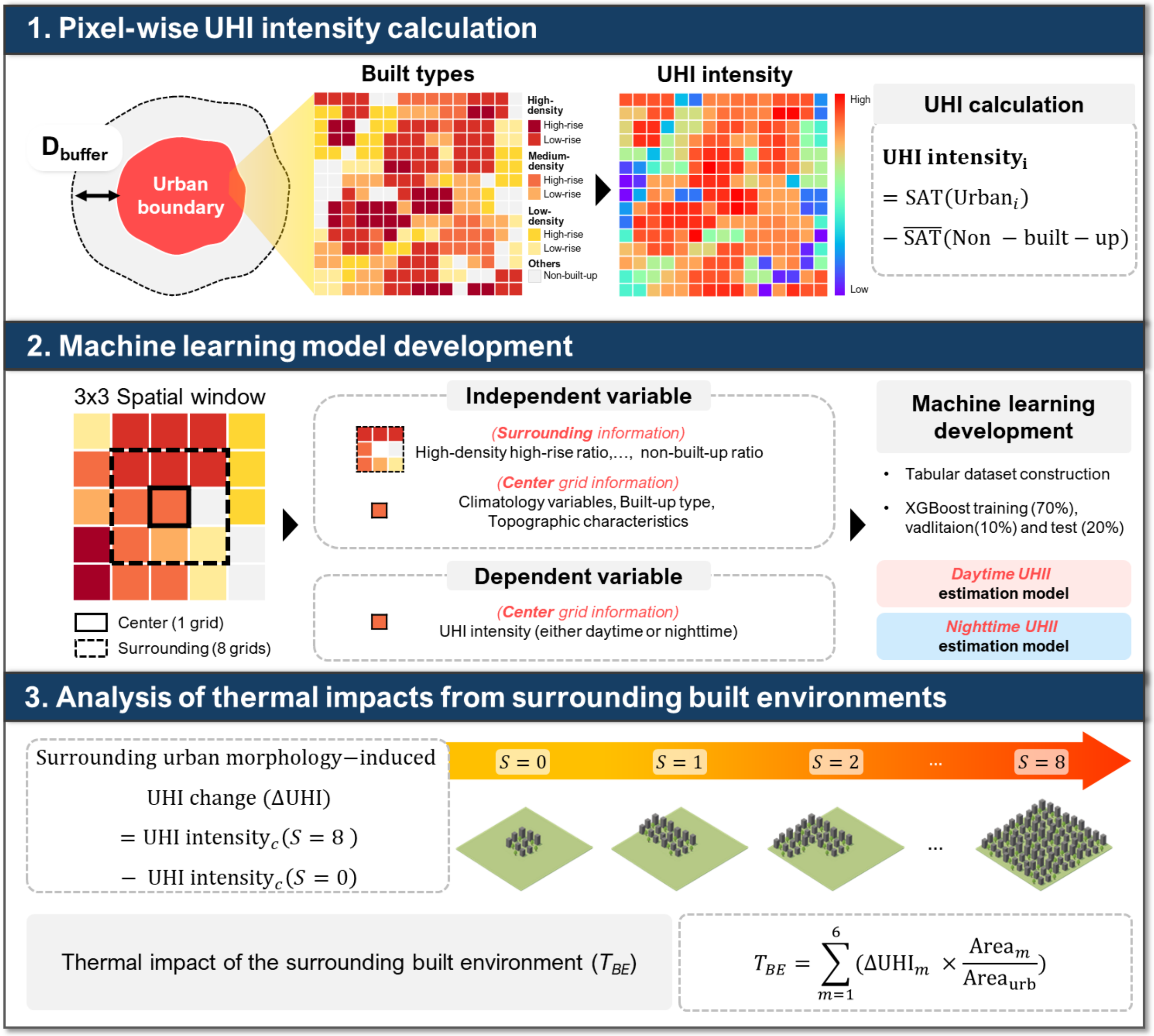

Fig. 1 | Framework for assessing the combined effect of climate and urban morphology on urban heat. The framework combines urban morphology-based canopy urban heat island (UHI) estimation with machine learning to quantify the thermal impact of the surrounding urban structures. Pixel-level UHI intensity is defined as the near-surface air temperature (SAT) difference between each built-up pixel i and non-built-up areas. Using a 3×3 spatial window, the eXtreme Gradient Boosting (XGBoost) model predicts center-pixel UHI from surrounding built-up compositions and local environmental variables. Surrounding urban morphology-induced UHI change (ΔUHI) is defined as the difference in modeled UHI intensity between six built-up types surrounded by the same built form and those surrounded by non-built-up. Here, UHI intensity_c denotes the UHI intensity at the central pixel; S indicates the number of surrounding pixels classified as a specific built-up type. Thermal impact of the surrounding built environment (T_{BE}) is calculated by aggregating surrounding built-up type thermal impacts across six built-up types, weighted by their proportional coverage within each city; ΔUHI_m indicates ΔUHI associated with built-up type m, and Area_m is the area of built-up type m, and Area_{urb} denotes the total buffered area. This calculation is performed independently for each city.

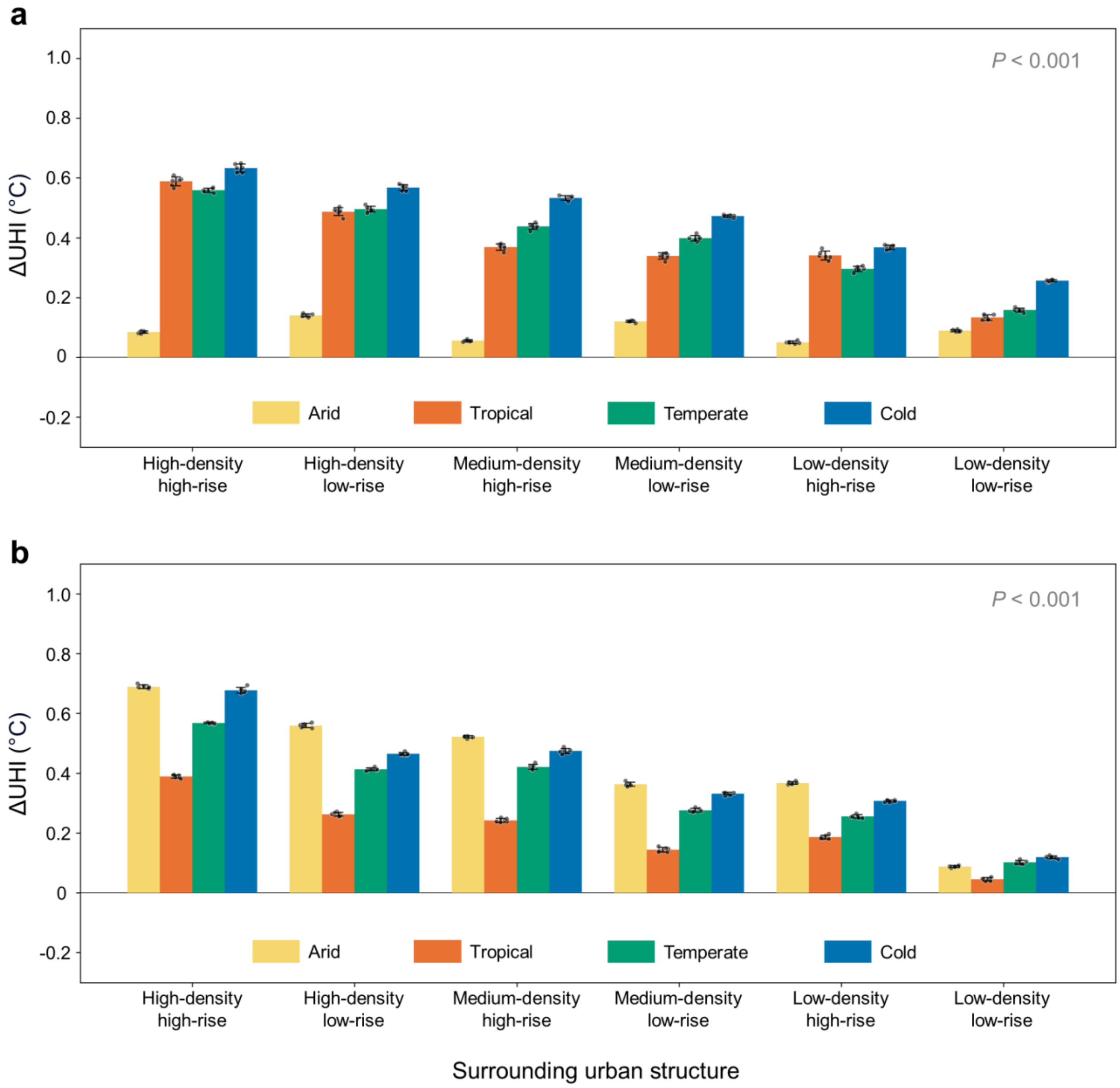

Fig. 2 | Surrounding urban morphology-induced urban heat island change (ΔUHI) across climate zones. a, b ΔUHI during the daytime (**a**) and nighttime (**b**), defined as the change in canopy urban heat island (UHI) intensity when adjacent land cover transitions from non-built-up to a given built-up type. All six built-up types were applied as central pixels; ΔUHI represents the mean thermal influence of each built-up type, averaged across all combinations of central and surrounding built-up types. Bars indicate the average magnitude of ΔUHI in arid (403 cities), tropical (549 cities), temperate (946 cities), and cold (315 cities) climate zones. Dots indicate the mean ΔUHI values for each central built-up type, and error bars represent the standard deviation across these types. *P* values are from two-way ANOVA.

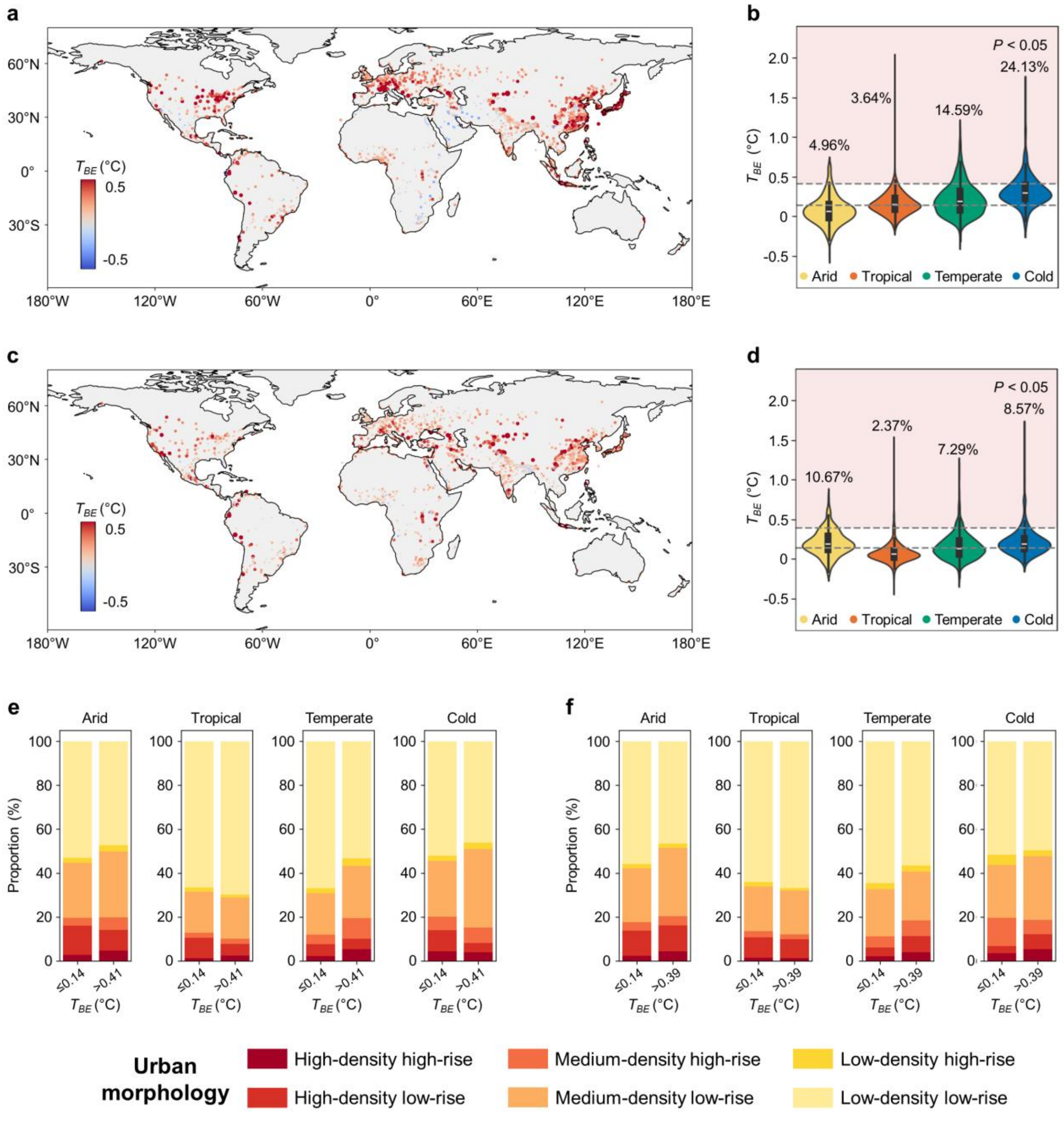

Fig. 3 | Spatial and structural distribution of thermal impact of the surrounding built environment (T_{BE}). a Global distribution of daytime T_{BE} across 2,213 global cities, with dot color and size indicating T_{BE} intensity. **b** Violin plots display the distribution of daytime T_{BE} values stratified by climate zone. Within each violin, the white line indicates the median, the box indicates the interquartile range (IQR), and the whiskers extend to 1.5 × IQR. Horizontal dashed lines indicate category thresholds determined using the Jenks natural breaks method; red-shaded areas correspond to the high-T_{BE} category. Numbers above each violin indicate the proportion of cities classified as high T_{BE} within each climate zone. P values are based on the Kruskal–Wallis H test. **e** Proportional composition of six built-up types for cities grouped by daytime T_{BE} category (high: > 0.41 °C; low: ≤ 0.14 °C) within each climate zone. **c, d,** and **f** are the same as **a, b,** and **e** but for nighttime T_{BE}. Basemap from Natural Earth (https://www.naturalearthdata.com).

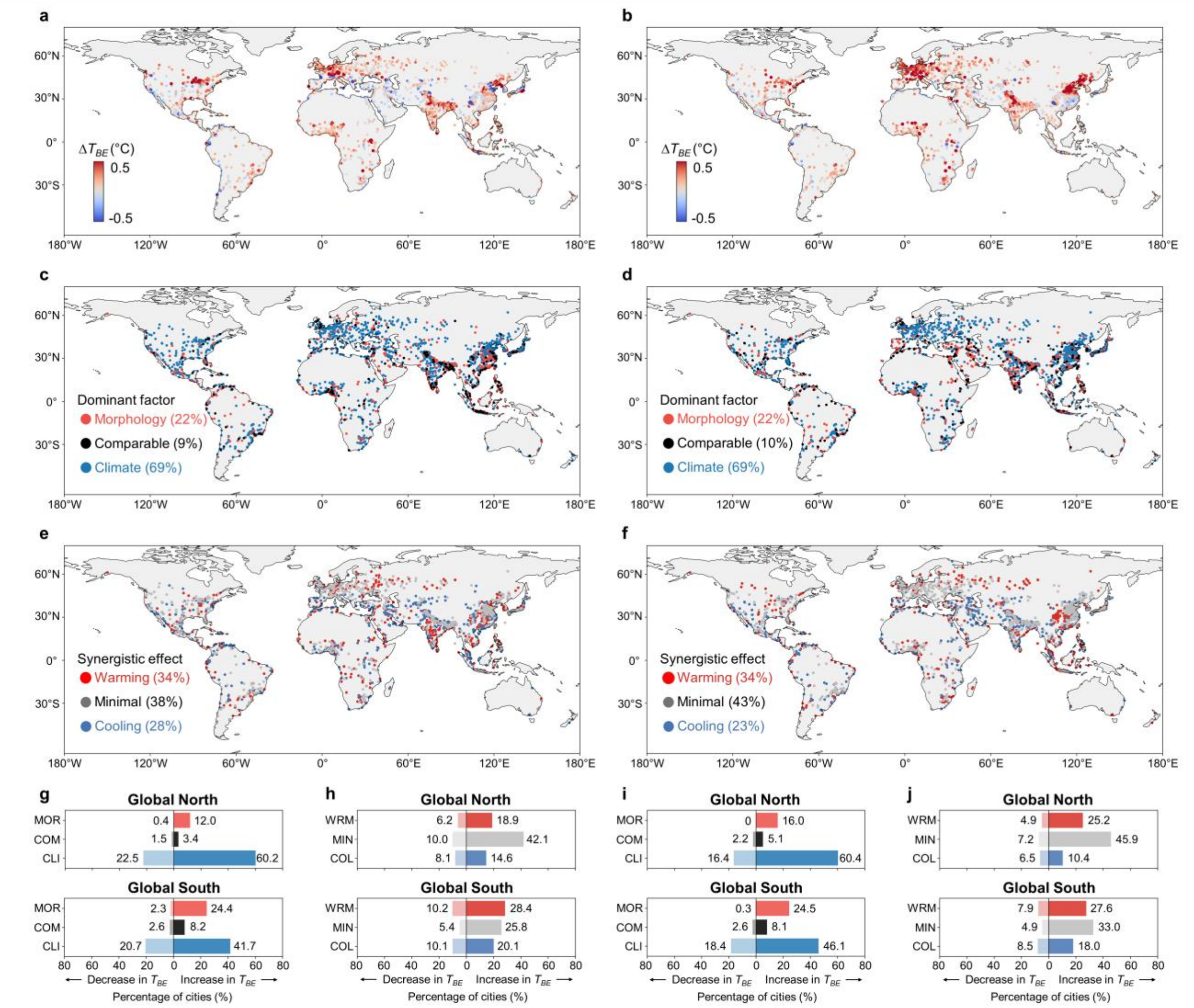

Fig. 4 | Global distribution of projected changes in the thermal impact of the surrounding built environment (T_{BE}) and their attribution to climate, morphology, and interaction under Shared Socioeconomic Pathways 5 (SSP5). a, b Spatial distribution of projected differences in T_{BE} (ΔT_{BE}) between present-day (2020) and future (2050) conditions for daytime (**a**) and nighttime (**b**). Positive values indicate intensification of T_{BE}, whereas negative values indicate weakening. **c, d** Spatial distribution of the dominant driver of projected T_{BE} change for daytime (**c**) and nighttime (**d**): morphology (MOR), comparable (COM), or climate (CLI). Numbers indicate the proportion of all 2,213 cities assigned to each category. Dominance was quantified using a normalized score based on the relative absolute magnitudes of the climate-only and morphology-only contributions. The climate-only contribution was calculated by applying future long-term climate conditions while holding urban morphology at its present state, whereas the morphology-only contribution was calculated by applying future urban morphology while holding climate constant. Cities were classified as climate when the score was > 0.1, morphology when it was < −0.1, and comparable when it fell within ±0.1 of zero. **e, f** Synergistic effects between climate change and urban morphological change on projected daytime (e) and nighttime (f) T_{BE} change, calculated as the residual between projected T_{BE} under future conditions and the sum of the climate-only and morphology-only changes. Numbers indicate the percentage of all 2,213 cities assigned to each synergistic class. Synergistic effects were defined using the same threshold: warming (WRM) for values > 0.1, cooling (COL) for values < −0.1, and minimal (MIN) for values within ±0.1. **g, h** Percentage of cities in each dominant-driver category (**g**) and synergistic-effect category (**h**) for the Global North and Global South under daytime conditions. Leftward bars from zero (lighter shading) indicate cities with decreasing T_{BE} and rightward bars from zero (darker shading) indicate cities with increasing T_{BE}. **i, j** Same as **g** and **h**, but for nighttime conditions. Basemap from Natural Earth (https://www.naturalearthdata.com).

Editorial Summary

This study shows that global urban heat is shaped by both climate and urban morphology. Climate change dominates future urban heat in most cities, while urban morphology remains crucial for regional differences and targeted adaptation strategies.

Peer review information: *Nature Communications* thanks Rey Jalbuena, Deniz Erdem Okumus, and the other, anonymous, reviewer for their contribution to the peer review of this work. A peer review file is available.